The Structural Origin of Nonplanar Heme Distortions in Tetraheme Ferricytochromes c_3[†]

Jian-Guo Ma,[‡] Jun Zhang,[‡] Ricardo Franco,[§] Song-Ling Jia,[‡] Isabel Moura,[§] José J. G. Moura,[§] Peter M. H. Kroneck,[||] and John A. Shelnutt*[,‡]

Materials Theory and Computation Department, Sandia National Laboratories, Albuquerque, New Mexico 87185-1349, Department of Chemistry, University of New Mexico, Albuquerque, New Mexico 87131, Centro de Química Fina e Biotecnologia, Departamento de Química, Faculdade de Ciências e Tecnologia, Universidade Nova de Lisboa, 2825 Monte de Caparica, Portugal, and Fakultät für Biologie, Universität Konstanz, D-78457 Konstanz, Germany

Received May 20, 1998; Revised Manuscript Received July 8, 1998

ABSTRACT: Resonance Raman (RR) spectroscopy, molecular mechanics (MM) calculations, and normal-coordinate structural decomposition (NSD) have been used to investigate the conformational differences in the hemes in ferricytochromes c_3. NSD analyses of heme structures obtained from X-ray crystallography and MM calculations of heme-peptide fragments of the cytochromes c_3 indicate that the nonplanarity of the hemes is largely controlled by a fingerprint peptide segment consisting of two heme-linked cysteines, the amino acids between the cysteines, and the proximal histidine ligand. Additional interactions between the heme and the distal histidine ligand and between the heme propionates and the protein also influence the heme conformation, but to a lesser extent than the fingerprint peptide segment. In addition, factors that influence the folding pattern of the fingerprint peptide segment may have an effect on the heme conformation. Large heme structural differences between the *baculatum* cytochromes c_3 and the other proteins are uncovered by the NSD procedure [Jentzen, W., Ma, J.-G., and Shelnutt, J. A. (1998) *Biophys. J. 74*, 753−763]. These heme differences are mainly associated with the deletion of two residues in the covalently linked segment of hemes 4 for the *baculatum* proteins. Furthermore, some of these structural differences are reflected in the RR spectra. For example, the frequencies of the structure-sensitive lines (ν_4, ν_3, and ν_2) in the high-frequency region of the RR spectra are lower for the *Desulfomicrobium baculatum* cytochromes c_3 (Norway 4 and 9974) than for the *Desulfovibrio (D.) gigas*, *D. vulgaris*, and *D. desulfuricans* strains, consistent with a more ruffled heme. Spectral decompositions of the ν_3 and ν_{10} lines allow the assignment of the sublines to individual hemes and show that ruffling, not saddling, is the dominant factor influencing the frequencies of the structure-sensitive Raman lines. The distinctive spectra of the *baculatum* strains investigated are a consequence of hemes 2 and 4 being more ruffled than is typical of the other proteins.

Cytochrome c_3 is a tetraheme protein found in sulfate-reducing bacteria, which are capable of using sulfate of thiosulfates as the terminal electron acceptor. X-ray crystal structures of cytochromes c_3 from the organisms *Desulfovibrio gigas* (*1*), *D.*[1] *vulgaris* [Hildenborough (*2*, *3*) and Miyazaki (*4*)], *D. desulfuricans* (*5*), and *Desulfomicrobium baculatum* (*6*, *7*) have been solved, showing that the general outlines of their protein structure are essentially the same. Specifically, the X-ray structures indicate that the overall protein folding is conserved (*5*). The structural similarity occurs although the amino acid sequences exhibit as little as about 20% identity, and this mostly resulting from the eight conserved histidine axial ligands and eight cysteine residues linked to the hemes. A recent analysis of the crystal structures provides a more detailed understanding of the structures of the hemes in these proteins (*8*). It was found that the conformations of the four hemes are different from each other, but the structures are conserved for corresponding hemes. The exception is hemes 4, which exhibits a very different structure for *Dsm. baculatum* cytochromes c_3. In the present work, we explore the structural origin of the heme distortions in these proteins.

Nonplanar distortions of tetrapyrroles are prevalent in the hemes of hemoproteins, the pigments of photosynthetic proteins, and cofactor F_{430} of methylreductase (*9*). The nonplanarity of these porphyrin cofactors is believed to influence the biological activity of the proteins, in part, because the porphyrin deformations are often conserved within functional classes of proteins (*8*, *9*). The hemoproteins provide a representative example of the occurrence of nonplanar porphyrins in proteins. It has been recognized for about 10 years that the hemes in many hemoproteins are highly distorted from planarity and that these nonplanar

[†]Sandia is a multiprogram laboratory operated by Sandia Corporation, a Lockheed Martin Company, for the United States Department of Energy under Contract DE-AC04-94DP85000. I.M., J.J.G.M., and R.F. want to thank the PRAXIS Program for financial support.

* To whom correspondence should be addressed.
[‡] Sandia National Laboratories and University of New Mexico.
[§] Universidade Nova de Lisboa.
[||] Universität Konstanz.

[1] Abbreviations: RR, resonance Raman; MM, molecular mechanics; NSD, normal-coordinate structural decomposition; MP, microperoxidase; *D.*, *Desulfovibrio*; *Dsm.*, *Desulfomicrobium*.

S0006-2960(98)01189-1 CCC: $15.00
Published on Web 08/20/1998

distortions might play a role in their biological function (*10*−*15*). Further, by using a new normal-coordinate structural decomposition (NSD) procedure (*8*, *16*, *17*) for characterizing and quantifying these heme distortions, our group has shown that these distortions are often of different types for hemoproteins with different functions. However, often the types of distortion are conserved for proteins with the same function but isolated from different species (*8*, *18*). Since nonplanar distortion is energetically unfavorable for Fe porphyrins (*19*), conservation of the heme conformation strongly suggests that the biological function of hemoproteins might be modulated by protein control over the conformation of the heme prosthetic group.

A structural mechanism for inducing the nonplanarity of the heme group has been suggested for mitochondrial cytochromes *c* based on NSD analysis of X-ray crystal structures of native and mutant proteins (*8*) and resonance Raman spectroscopy and molecular simulations of nickel-reconstituted cytochrome *c* (*20*) and model heme-peptides (*21*). These studies are consistent with a relatively small covalently linked protein segment causing most of the distortion of the heme. This protein segment includes the cysteines, the amino acids between the cysteines, and the adjacent histidine ligand (*8*, *20*). MM calculations were also employed to explore the influence of the conformation of the heme-linked protein segment on the heme distortion. The energy-optimized structures consisting of the heme and the covalently linked pentapeptide were analyzed using the NSD method to simply specify the type of heme distortion resulting from these interactions. The interaction between the pentapeptide and the heme accounts for the major deformation contributing to the heme conformation.

The heme-linked segment is thought to be important also in causing the distortion of the hemes in cytochromes c_3. Nevertheless, important questions remain concerning the detailed mechanism of the protein segment's interaction with the heme and the possible influence of the heme distortion on biological function. In this work, MM calculations and NSD analysis of heme-peptide fragments from different strains show in some detail how mainly this small protein segment controls the heme nonplanarity. The distal histidine and H-bond interactions with the propionates are also shown to influence the heme conformation but to a lesser extent.

Solution RR spectra of cytochromes c_3 from the different organisms provide experimental evidence for the structural differences in the hemes that are observed in the X-ray crystal structures. The frequencies of the structure-sensitive Raman lines are shown to be indicative of the magnitude of the ruffling deformation only, allowing the assignment of each heme in the crystal structure to a subline of the Raman lines.

The nonplanarity of the porphyrin has been shown to influence the redox potential of the porphyrin ring (*9*). Fajer et al. (*11*) and Ravikanth and Chandrashekar (*22*) demonstrated that nonplanar porphyrins are easier to oxidize and harder to reduce than planar porphyrins. Microscopic redox potentials determined for cytochromes c_3 from electrochemical methods and spectroelectrochemical data show that the four hemes exhibit a range of redox potentials (*23*−*28*). These variations in the redox potentials are discussed in terms of the different magnitudes of the nonplanar deformations of the hemes.

MATERIALS AND METHODS

Materials. Samples of cytochromes c_3 from different strains were prepared by the following procedures: cytochromes c_3 from *D. gigas* (*29*), *D. vulgaris* Hildenborough (*30*), *D. desulfuricans* ATCC 27774 (*31*), and *Dsm. Baculatum* [strains Norway 4 (*32*) and 9974 (*27*)] were purified from the respective bacterial crude extracts following published procedures. The purified proteins were dialyzed overnight against 10 mM Tris HCl at pH 7.0 and lyophilized. The lyophilized proteins were then dissolved in 50 mM phosphate buffer solution at pH 7.0. The concentration used for the Raman spectra was 20 μM as determined spectrophotometrically.

Resonance Raman Spectroscopy. RR spectra were obtained using a dual-channel spectrometer described previously (*33*). The solution spectra of proteins from two different strains were obtained simultaneously in separate compartments of a cylindrical rotating quartz cell. Rotation of the Raman cell at 50 Hz prevented local heating of the sample even with incident laser powers were as high as 100 mW. A krypton (Coherent, INNOVA 20) ion laser provided the excitation wavelength of 406.7 nm in the Soret band regions of the absorption spectrum.

Laser powers were 50 mW at the quartz cell. The scattered light was collected in a 90° scattering geometry. For each scan, counts were accumulated for 1 s at each point of the spectrum for which the spectrometer step size was 0.3 cm^{-1} for each data point. All Raman spectra were taken at room temperature. Sample integrity was monitored by examination of selected single scans of the Raman spectrum obtained during signal averaging and by UV−vis absorption spectra taken before and after exposure to laser light. No degradation of the sample was observed for all measurements.

The peak positions of the Raman lines were obtained by decomposing the Raman spectra into Lorentzian line shapes using a nonlinear, least-squares curve-fitting program (PeakFit, Jandel Scientific) in which the peak frequency, peak intensity, line width, and a linear background were allowed to vary. A Gaussian contribution to the line width is not usually required for hemes. Four sublines with shared areas were used to fit the ν_{10} line, assuming that each of the four hemes has an equal contribution to the spectrum. The line widths of the nonplanar forms (with lower frequency) were also shared in the curve fitting, while the line width of the nearly planar form (at highest frequency) was allowed to vary independently. This was done simply to allow as many parameters to vary as is statistically supported by the quality of the Raman data sets. When all line widths were allowed to vary (while maintaining equal areas), the spectral decompositions give similar results. Similarly, the analysis with all line widths equal gives statistically insignificant differences in the frequencies of the sublines and these compare favorably with the averages for six data sets (Table 3), with all variations within the statistical uncertainty. The ν_3 line was also decomposed into four Lorentzian sublines with shared areas and widths.

Molecular Mechanics Calculations. MM calculations were carried out using modified version of POLYGRAF 3.21 software (Molecular Simulations, Inc.) and a hybrid force field based on the DREIDING II force field parameters (*34*).

Table 1: Covalently Linked Peptide Segments of the Four Heme Groups in Cytochromes c_3 from *D. vulgaris* (Hildenborough and Miyazaki), *D. gigas*, *D. desulfuricans* (ATCC 27774), and *Dsm. baculatum* (Norway 4), Dimeric *cc*3, and the Y73E Mutant of *cc*3[a]

	D. vulgaris, Hildenborough		*D. vulgaris*, Miyazaki (2cdv)	*D. gigas* (1wad)	*D. desulfuricans*, ATCC 27774 (3cyr)	*Dsm. baculatum*		
	(2cth)	(2cym)				Norway 4 (2cy3)	Norway 4 (*cc*3) (1czj)	*cc*3 (Y73E) (1aqe)
heme 1	C**GD**− −C	C**GD**− −C	C**GD**− −C	C**DD**− −C	C**VT**− −C	C**VQ**− −C	C**QQ**− −C	C**QQ**− −C
heme 2	C**GTAG**C	C**GTAG**C	C**ATAG**C	C**TTDG**C	C**GSSG**C	C**TTSG**C	C**MTEG**C	C**MTEG**C
heme 3	C**VG**− −C	C**VG**− −C	C**VG**− −C	C**IS**− −C	C**LA**− −C	C**ID**− −C	C**VG**− −C	C**VG**− −C
heme 4	C**KKSK**C	C**KKSK**C	C**KGSK**C	C**KGSA**C	C**AKSK**C	C− **G**−**K**C	C**N**− **S**−C	C**N**− **S**−C

[a] All the fifth and sixth axial ligands of the heme iron atoms are histidine nitrogen atoms. One−letter symbols are used for the amino acids.

Table 2: Frequencies (cm^{-1}) of Selected Resonance Raman Lines for Ferricytochromes c_3 in 50 mM Phosphate Buffer at pH 7.0 with 406.7 nm Excitation

cytochromes c_3	ν_4	ν_3	ν_2
D. gigas	1372.7	1503.8	1587.3
D. vulgaris	1372.5	1502.5	1586.4
D. desulfuricans			
ATCC 27774	1372.9	1502.5	1586.6
Essex 6	1373.2	1503.5	1586.6
Dsm. baculatum			
Norway 4	1372.2	1501.3	1585.6
9974	1372.3	1501.6	1585.6

Specifically, the DREIDING II force field was modified to include atom types specific to the porphyrin macrocycle (*35*). Force constants for the macrocycle atom types were obtained from normal coordinate analyses of nickel porphyrins (*36*−*38*). The equilibrium bond lengths and some bond angles were varied so that the energy-optimized structure of nickel(II) octaethylporphyrin (NiOEP) obtained using the extended DREIDING force field matched the planar crystal structures of NiOEP as closely as possible. DREIDING II parameters were used for all of the nonbonding interactions and for the internal force field of the peripheral substituents of the porphyrin. The out-of-plane force constants from the normal coordinate analyses are reduced by 50%, greatly improving the ability to correctly predict the degree of nonplanarity and relative energies of various conformers (*19*, *39*−*42*). The 50% reduction in the out-of-plane force constants is necessary (*39*) because the in-plane and out-of-plane normal coordinate analyses (*36*−*38*) were done independently, and the in-plane force constant has an out-of-plane component not included in the out-of-plane normal coordinate analysis.

For the central Fe^{3+} atom type, the equilibrium bond distance and the homonuclear bond separation of the M−N bond was set to 1.975 and 4.54 Å, respectively, as in previous calculations (*43*). The solvent dielectric constant was set to 79 to mimic the solvent conditions.

The initial structures used in the MM calculations were constructed from the crystal structures of the corresponding protein. These structures are either MP-5 or MP-7 with and without the sixth histidine ligand. Parts of the protein are selectively fixed in the energy minimization to mimic specific interactions between the protein moiety and the heme group. The minimized structures were then decomposed using the NSD method (vide infra) to obtain the specific out-of-plane and in-plane displacements of the porphyrin macrocycle used for comparison with NSD results for the crystal structures.

Normal-Coordinate Structural Decomposition. Jentzen and Shelnutt (*16*) have developed a method for classifying and quantifying the out-of-plane and in-plane distortions of the porphyrin macrocycle. In its simplest form, the NSD method uses a linear combination of the six lowest-frequency out-of-plane normal coordinates of the macrocycle, one for each D_{4h} symmetry type, to simulate the macrocyclic distortion. In most cases, out-of-plane distortions of the macrocycle can be described adequately by summing just these displacements. Pure displacements along these coordinates correspond to the commonly observed symmetric deformations seen in X-ray crystal structures. The amounts of the saddling (*sad*), ruffling (*ruf*), doming (*dom*), waving [*wav(x)* and *wav(y)*], and propellering (*pro*) deformation types required to simulate the observed out-of-plane distortions of the porphyrin macrocycle are determined for a given structure by the NSD procedure.

RESULTS AND DISCUSSION

Molecular Mechanics Calculations. MM calculations greatly aid in locating the forces in the protein moiety that cause the nonplanar macrocyclic distortion (*20*). In our previous work (*8*), analysis of the influence of natural sequence variation and engineered mutations for *c*-type cytochromes suggested that the source of the heme distortion is most likely concentrated in a small segment of the protein, specifically the covalently linked peptide segment. Also, the electronic and steric interactions with axial ligands, the multitude of nonbonding interactions with nearby amino acid residues, and the hydrogen bonds with the heme are probably similarly important (*8*, *20*).

To further examine this structural hypothesis, MM calculations were carried out on each of the four hemes of ferricytochromes c_3 with their covalently linked peptide segment. During the minimization, the protein component was frozen in place at the X-ray structure positions and the heme atoms were allowed to move in the minimization subject to the interaction with the fixed protein segment. In another series of calculations, the fixed sixth ligand was included, and in third series, the oxygen atoms of the two propionates were also fixed in order to evaluate the effect of hydrogen bonds to the protein. Finally, in selected cases, the heme was energy optimized with the entire ferricytochrome c_3 protein component fixed. All energy-optimized heme structures were then decomposed using the NSD method and the results were compared to the NSD results for the cytochrome c_3 X-ray crystal structures.

Figure 1 shows the energy-optimized structure of heme 2 of *D. gigas* (1wad) cytochrome c_3 with the cysteine-linked segment and the sixth histidine ligand, illustrating the part of the protein that was used in the calculations. For this structure, the protein segment and the oxygen atoms on the

Table 3: Frequencies and Line Widths (cm^{-1}) for the ν_{10} and ν_3 Raman Lines of Cytochromes c_3 from *D. gigas*, *D. vulgaris* Hildenborough, *D. desulfuricans* (ATCC 27774 and Essex 6), and *Dsm. baculatum* (Norway 4 and 9974)[a,b]

	$\nu_{10}{}^1$		$\nu_{10}{}^2$		$\nu_{10}{}^3$		$\nu_{10}{}^4$	
cytochromes c_3	frequency	line width[c]	frequency	line width[c]	frequency	line width[c]	frequency	line width
D. gigas	1631.5 ± 0.9	14.9 ± 1.6	1634.8 ± 0.7	14.9 ± 1.6	1638.5 ± 1.2	14.9 ± 1.6	1640.1 ± 1.0	9.9 ± 1.2
D. vulgaris	1632.1 ± 0.6	11.4 ± 0.6	1634.4 ± 0.7	11.4 ± 0.6	1636.0 ± 0.6	11.4 ± 0.6	1636.9 ± 0.5	9.2 ± 0.8
D. desulfuricans								
ATCC 27774	1631.4 ± 0.3	8.6 ± 0.5	1634.5 ± 0.3	8.6 ± 0.5	1636.9 ± 0.5	8.6 ± 0.5	1639.9 ± 0.2	8.0 ± 0.5
	(1631.5 ± 0.8)[d]	(9.2 ± 1.3)	(1634.9 ± 0.4)	(9.2 ± 1.3)	(1636.8 ± 0.6)	(9.2 ± 1.3)	(1639.8 ± 0.2)	(8.8 ± 1.1)
	[1631.6 ± 0.3][e]	[7.5 ± 0.9]	[1635.5 ± 0.4]	[7.5 ± 0.9]	[1637.1 ± 0.8]	[7.5 ± 0.9]	[1640.3 ± 0.4]	[7.7 ± 1.0]
Essex 6	1631.1 ± 0.3	10.0 ± 0.8	1636.2 ± 1.1	10.0 ± 0.8	1636.2 ± 1.1	10.0 ± 0.8	1640.0 ± 0.4	9.2 ± 0.5
Dsm. baculatum								
Norway 4	1625.4 ± 0.2	11.4 ± 0.5	1633.7 ± 1.1	11.4 ± 0.5	1633.7 ± 1.0	11.4 ± 0.5	1638.0 ± 0.2	8.3 ± 0.4
	[1626.9 ± 0.6]	[10.5 ± 1.6]	[1634.7 ± 1.1]	[10.5 ± 1.6]	[1634.7 ± 1.1]	[10.5 ± 1.6]	[1638.2 ± 0.6]	[7.5 ± 1.1]
9974	1625.5 ± 0.3	11.2 ± 0.5	1633.4 ± 1.1	11.2 ± 0.5	1633.8 ± 1.0	11.2 ± 0.5	1637.7 ± 0.3	8.3 ± 0.9

	$\nu_3{}^1$		$\nu_3{}^2$		$\nu_3{}^3$		$\nu_3{}^4$	
cytochromes c_3	frequency	line width[c]	frequency	line width[c]	frequency	line width[c]	frequency	line width[c]
D. gigas	1498.1 ± 0.2	7.6 ± 0.4	1502.3 ± 0.2	7.6 ± 0.4	1505.5 ± 0.2	7.6 ± 0.4	1508.8 ± 0.2	7.6 ± 0.4
D. vulgaris	1497.7 ± 0.2	7.5 ± 0.3	1501.7 ± 0.2	7.5 ± 0.3	1503.5 ± 0.2	7.5 ± 0.3	1507.0 ± 0.2	7.5 ± 0.3
D. desulfuricans								
ATCC 27774	1497.4 ± 0.2	8.0 ± 0.4	1501.4 ± 0.2	8.0 ± 0.4	1503.8 ± 0.2	8.0 ± 0.4	1507.8 ± 0.2	8.0 ± 0.4
Essex 6	1498.4 ± 0.2	7.9 ± 0.3	1502.4 ± 0.2	7.9 ± 0.3	1504.8 ± 0.2	7.9 ± 0.3	1508.9 ± 0.2	7.9 ± 0.3
Dsm. baculatum								
Norway 4	1496.6 ± 0.2	8.7 ± 0.4	1500.8 ± 0.4	8.7 ± 0.4	1501.8 ± 0.4	8.7 ± 0.4	1506.6 ± 0.2	8.7 ± 0.4
9974	1496.6 ± 0.2	8.9 ± 0.5	1501.3 ± 0.7	8.9 ± 0.5	1502.0 ± 0.7	8.7 ± 0.5	1506.9 ± 0.2	8.7 ± 0.5

[a] The peak area of four sublines was shared in the curve fitting. [b] The errors indicated represent confidence levels for the least-squares fits, not true errors. [c] The line width was shared in the curve fitting. [d] In parentheses, the average of six spectra; the uncertainties represent the largest variation in the fitting parameters. [e] In brackets, the frequencies and line widths of the four sublines of ν_{10} obtained with 413.1 nm excitation.

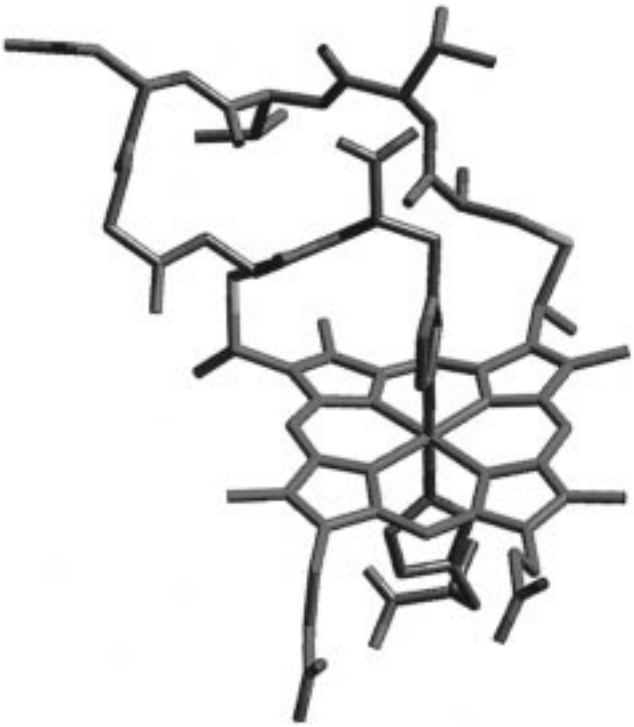

FIGURE 1: Representation of the protein segment used in the calculation, including the fingerprint peptide segment (two cysteines, the amino acids between the cysteines, and the proximal histidine), the heme, and the sixth histidine ligand.

propionates were fixed at their average crystallographic positions. As indicated in Figure 1, the heme and its immediate substituents (colored in green) are movable. The fixed peptide segment, histidine sixth ligand, and propionate oxygen atoms, in half-bond color, are perturbations that cause the nonplanarity of the heme.

For cytochromes c_3, there are two residues between the two cysteines for hemes 1 and hemes 3 and four residues for hemes 2 and hemes 4, except in the case of hemes 4 of the two *Dsm. baculatum* strains (2cy3 and 1czj) which have only two residues (*8*). We refer to these energy-optimized heme structures as either MP-5 or MP-7 depending on whether there are two residues or four residues between the cysteines. All MP-5 and MP-7 structures obtained from the crystal structures of *D. desulfuricans*, *D. gigas*, *D. vulgaris*, and *Dsm. baculatum* were energy minimized.

Normal-Coordinate Structural Decomposition. The description of the structure of a porphyrin ring in terms of the normal coordinates is a uniquely useful way of characterizing the macrocyclic structure. The mathematical procedure (*16*) projects out the displacements from an ideal geometry [a planar copper(II) porphine macrocycle] along the normal coordinates (*16*). Figure 2 illustrates 1 Å displacements along the lowest-frequency vibrational mode of each out-of-plane symmetry type. A 1 Å distortion means that the square root of the sum of the squares of the *z*-displacements from the mean plane is equal to 1. These normal deformations form a (minimal) basis for sufficiently characterizing the nonplanarity of the hemes of protein X-ray structures (*16*). The NSD method has been successfully used in decomposing and analyzing the structures of hemes of proteins in the Protein Data Bank (*8*) and of synthetic porphyrins (*39*). In this work, the energy-minimized structures of heme-peptides were analyzed using the NSD method to classify, quantify, and compare their out-of-plane distortions to the NSD results for the crystal structures.

Hemes 1. Figure 3 compares the structural decomposition results for hemes 1 of the X-ray crystal structures of cytochromes c_3 and also the energy-optimized structures of MP-5 taken from the corresponding protein. The heme

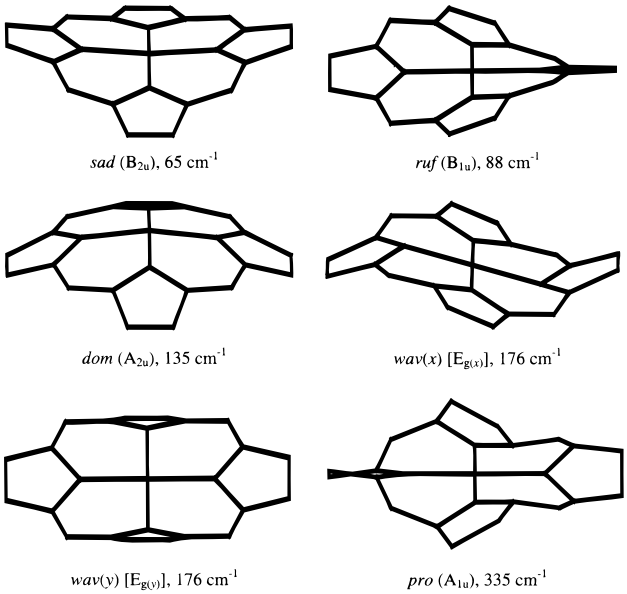

FIGURE 2: Illustrations of the lowest-frequency out-of-plane eigenvectors in coordinate space for each of the normal deformation [*sad*, *ruf*, *dom*, *wav(x)*, *wav(y)* and *pro*] used in describing the nonplanar distortions of the porphyrin macrocycle. Static displacements representing a 1 Å deformation along each lowest-frequency normal coordinate are shown (ref *16*).

numbering scheme is in the order of the cysteine residues along the primary sequence, i.e., hemes 1 has the lowest numbered cysteines and so forth (*6*). The first column (leftmost) in Figure 3 illustrates the NSD results for the X-ray crystal structures. A simple bar graph of the displacements clearly shows the similarities and differences in the structures of hemes 1 from different strains. The length of the bars represents the displacements along each out-of-plane symmetry type that gives the best fit to the X-ray structures. For example, the main contribution to the distortion of hemes 1 is a positive *ruf* deformation. Clearly, this contribution is highly conserved for the natural sequence variation, as is the small doming toward the histidine ligand. Some of the other types of deformations also contribute to the total heme distortion, but they are small and variable.

The NSD results for the energy-optimized structures of the hemes-1-peptides are illustrated in the second column from the left in Figure 3. It is clear that the calculations yield conformations similar to the X-ray structures in that the main type of distortion for hemes 1 is a positive *ruf* deformation. The positive *dom* deformation is also apparent for all of the minimized structures. Other deformations (positive *sad*, *wav*, and *pro*) are all small, except for saddling.

The third column of Figure 3 shows the NSD results for the MM calculations for which the fixed sixth ligand was also included in the energy minimization in addition to the peptide segment. For hemes 1, the most significant influences of the sixth ligand on the heme conformation are that the positive *ruf* deformation and the total distortion are reduced. There are also some changes in the magnitude of the *sad* deformation. Finally, fixing the oxygen atoms on the propionates of 6-coordinate MP-5 to mimic protein hydrogen bonding to the heme propionates results in further effects on the energy-optimized conformations of hemes 1 as shown in the fourth (rightmost) column of Figure 3. Addition of these perturbations, in the case of hemes 1, reduces the agreement between the X-ray and calculated structures.

Hemes 2. The structural decomposition results for the X-ray crystal and calculated structures of hemes 2 are compared in Figure 4. The conformations of hemes 2 in the crystal structures are mainly ruffled, and the ruffling is highly conserved for all of the different strains. A positive *wav(x)* deformation is also conserved in the crystal structures. For hemes 2 of cytochromes c_3 from strains *D. gigas* (1wad) and *Dsm. baculatum* (2cy3), a negative *sad* deformation is also important.

The NSD results for the energy-optimized hemes-2-peptides are shown in the second column of Figure 4. Like the hemes 2 of the crystal structures, the MM conformations of the hemes are dominated by a positive *ruf* deformation, and further the *ruf* deformation is conserved for all hemes-2-peptides. The magnitudes of the *dom*, *wav(x)*, *wav(y)*, and *pro* deformation are all small.

From the third column of Figure 4, the conformations of the energy-optimized 6-coordinate hemes 2 all have a positive *ruf* and a negative *sad* deformation. Addition of the fixed sixth ligand increases the negative *sad* deformation. Fixing the propionate oxygen atoms brings the minimized structures into close agreement with those of the crystal structures, as shown in the fourth column of Figure 4.

Hemes 3. The NSD results for hemes 3 in the crystal structures and various energy-optimized hemes-3-peptides are compared in Figure 5. The total distortion of hemes 3 in the crystal structures is typically smaller than that of the other hemes. Nevertheless, they all have small positive *ruf* and positive *sad* deformations (see first column of Figure 5). In contrast, the hemes of the energy-optimized five-coordinate hemes-3-peptides exhibit positive *ruf* and negative *sad* deformation as shown in the second column of Figure 5. Addition of the fixed histidine sixth ligand of hemes 3 reduces the negative *sad* deformation and increases the positive *ruf* deformation (third column of Figure 5). From the fourth column, the heme conformation becomes close to that of the crystal structures when the propionate oxygens are fixed in the minimization. All strains then have a positive *sad*, *ruf*, and *wav(x)* deformation like the hemes 3 of the crystal structures.

Hemes 4. There are two types of peptide segments for hemes 4, differing in the number of intervening amino acids between the cysteines. For hemes 4 from *D. desulfuricans*, *D. vulgaris*, and *D. gigas* strains, there are four while there are two for *Dsm. baculatum* (see Table 1). One would therefore expect a large difference in the conformation of the peptide and a concomitant difference in heme conformation. Indeed, examination of the structural decomposition results of hemes 4 of the crystal structures (first column of Figure 6) shows that two vastly different types of distortions are observed. For the proteins with four residues, the main deformation is positive *sad*; for the proteins with two residues, the predominant deformation is positive *ruf*. Comparison of the NSD results of the calculated 5-coordinate hemes-4-peptide structures with those of the crystal structures shows that just the small covalently linked protein segment induces these main types of deformation. In addition, adding the sixth histidine ligand and fixing the propionates make the resulting conformations even closer to the crystal structures.

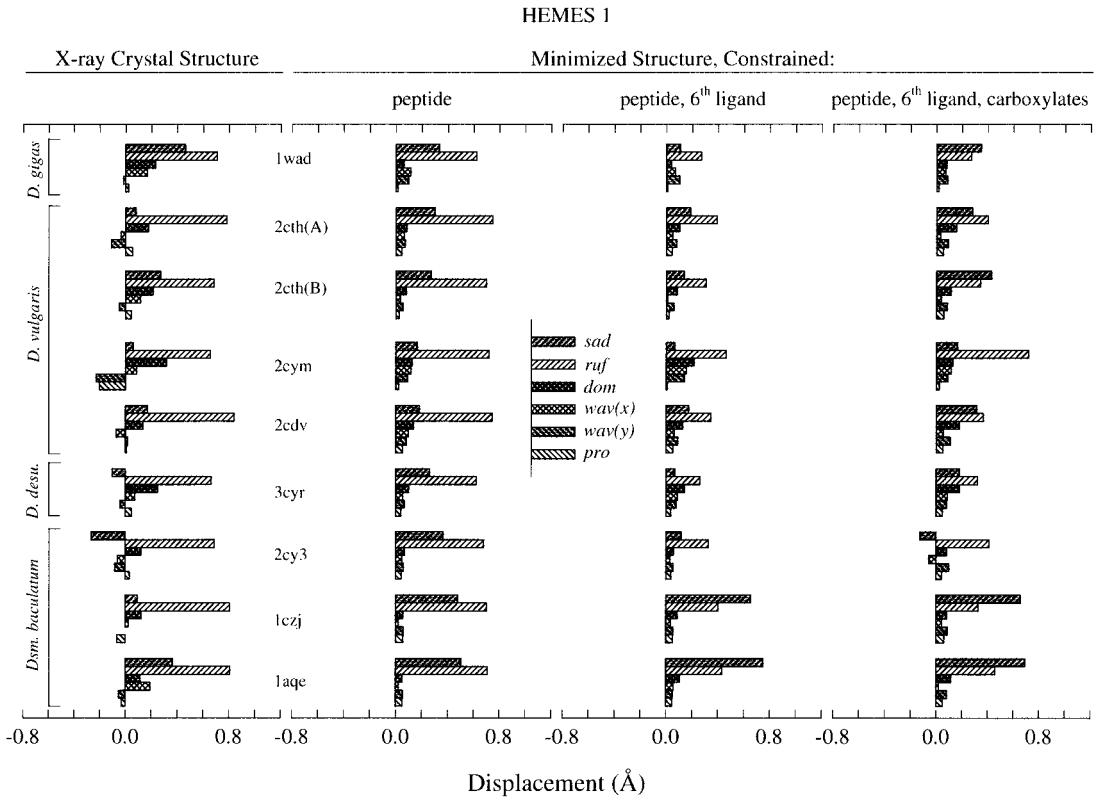

FIGURE 3: Out-of-plane displacements (minimal basis) for hemes 1 in the X-ray crystal and energy-optimized structures of cytochromes c_3 from different strains.

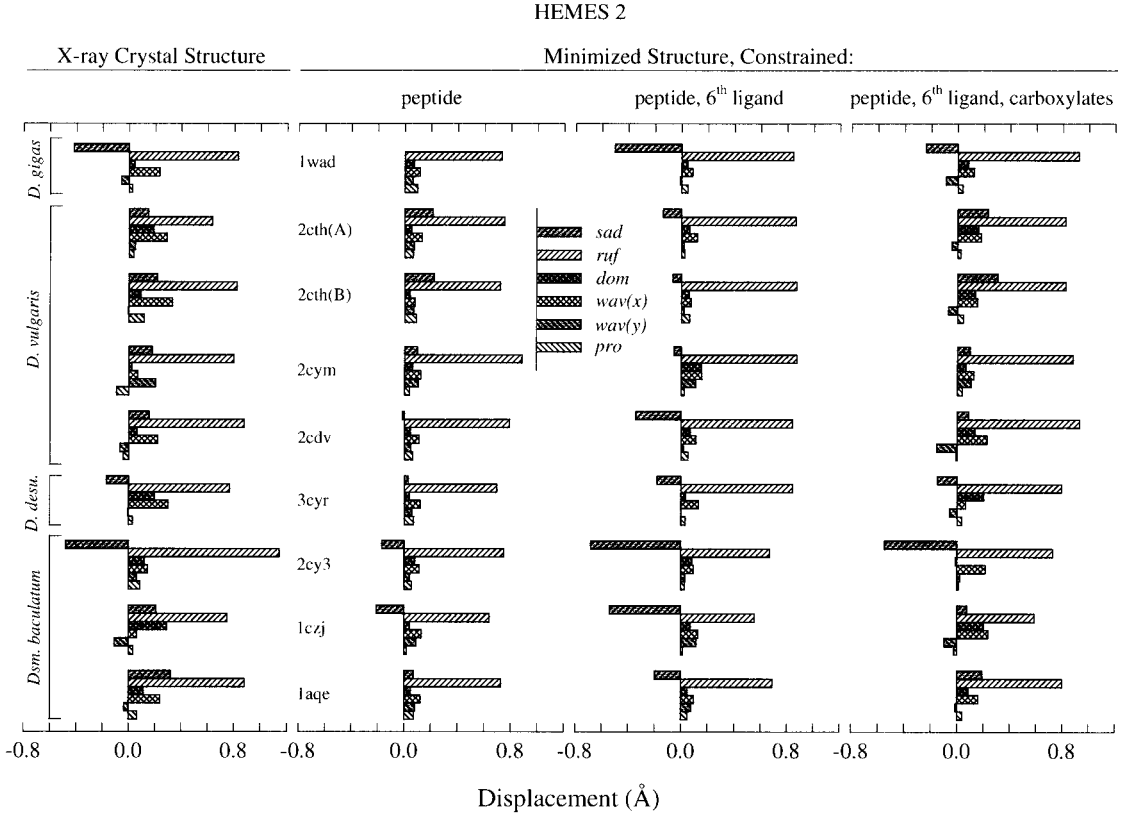

FIGURE 4: Out-of-plane displacements (minimal basis) for hemes 2 in the X-ray crystal and energy-optimized structures of cytochromes c_3 from different strains.

Resonance Raman Spectroscopy. RR spectra in the frequency range 200−1700 cm^{-1} of cytochromes c_3 from six different strains, including *D. gigas*, *D. vulgaris* Hildenborough, *D. desulfuricans* (ATCC 27774 and Essex 6), and *Dsm. baculatum* (Norway 4 and 9974), were obtained with 406.7 nm excitation. Many differences are observed for the

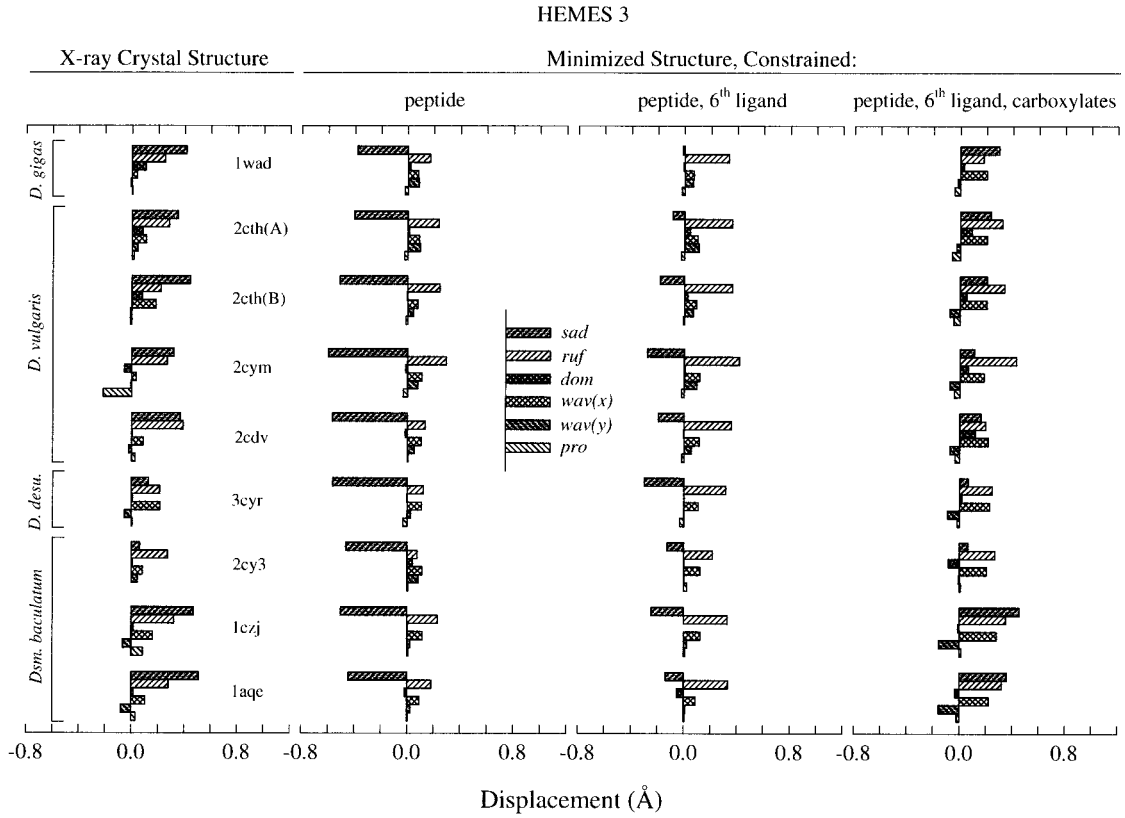

FIGURE 5: Out-of-plane displacements (minimal basis) for hemes 3 in the X-ray crystal and energy-optimized structures of cytochromes c_3 from different strains.

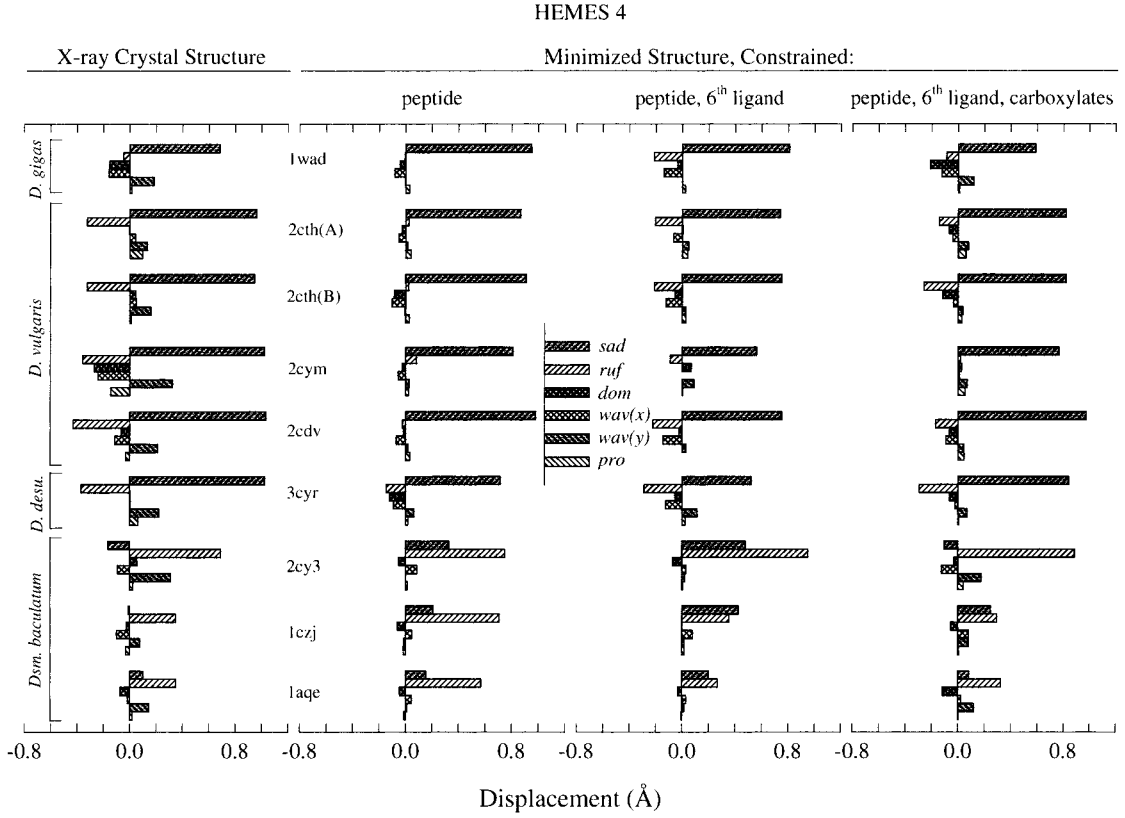

FIGURE 6: Out-of-plane displacements (minimal basis) for hemes 4 in the X-ray crystal and energy-optimized structures of cytochromes c_3 from different strain.

spectra of cytochromes c_3 from different strains in the low- and high-frequency regions. The richness of the *c*-type cytochromes resonance Raman spectra, especially in the low-frequency region, arises from the prominence of substituent modes, especially those of the 2,4-thioether substituents and those resulting from the activation of E_u and out-of-plane

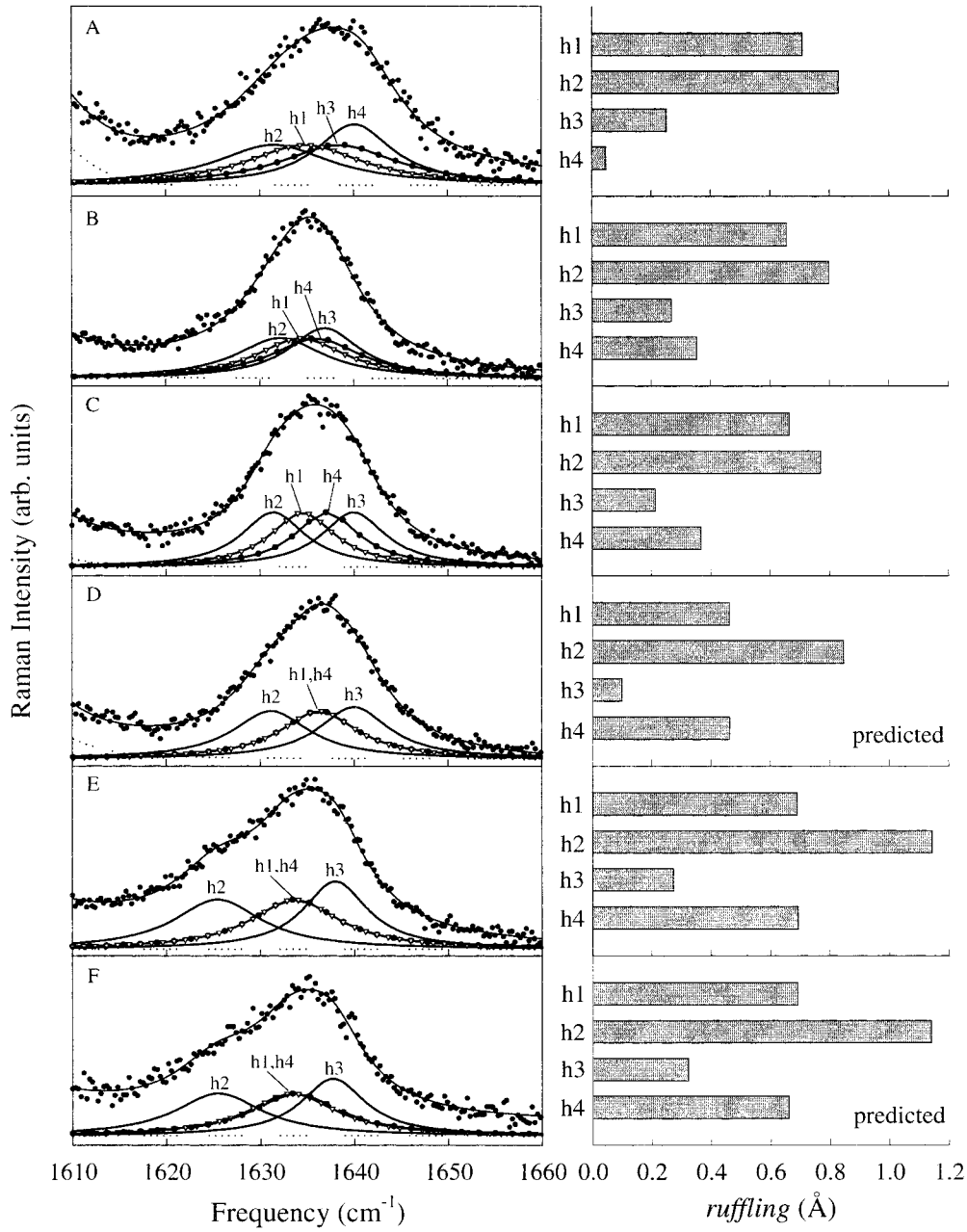

FIGURE 7: Lorentzian decomposition of the ν_{10} RR lines in the spectra of cytochromes c_3 from strains *D. gigas* (A), *D. vulgaris* Hildenborough (B), *D. desulfuricans* ATCC 27774 (C), *D. desulfuricans* Essex 6 (D), *Dsm. baculatum* Norway 4 (E), and *Dsm. baculatum* 9974 (F) with 406.7 nm excitation (right panel). The ruffling deformations (in angstroms) of each of the four hemes for the corresponding protein are shown in the bar graph in the left panel. The symbols h1, h2, h3, and h4 represent heme 1, heme 2, heme 3, and heme 4, respectively.

skeletal modes caused by protein-induced heme distortions (*36*−*38*, *44*). However, the spectra of this region are complicated with overlapping lines, making the interpretation of the spectra complex. The detailed interpretation of the Raman spectra in the low-frequency region will be presented in a forthcoming paper (*45*). In the present work, we focus on the high-frequency region (1300−1700 cm^{-1}) containing the structure-sensitive marker lines ν_4, ν_3, ν_2, and ν_{10}. The frequencies of ν_4, ν_3, ν_2, and the sublines of ν_{10} are listed in Tables 2 and 3, respectively. The Lorentzian decomposition results for ν_{10} are shown in the left panel of Figure 7. The bar graph in the right panel of Figure 7 shows the amount of the *ruf* deformation of each of the four hemes in the X-ray crystal structures of cytochromes c_3 from strains *D. gigas*, *D. vulgaris* Hildenborough, *D. desulfuricans* ATCC 27774, and *Dsm. baculatum* Norway 4. The predicted heme ruffling of the *D. desulfuricans* Essex 6 and *Dsm. baculatum* 9974 cytochromes c_3 are also given in Figure 7.

Since there are four hemes, in most cases it is difficult to say that the changes in the spectra are caused by a specific heme or by a specific deformation. Nevertheless, an analysis of the shape of ν_{10}, which exhibits the largest changes in the high-frequency region of the Raman spectra, does give information on the individual hemes. A detailed analysis of ν_{10} is possible most likely because it is the most sensitive to nonplanar distortion of the porphyrin (*20*). Of the other lines in the high-frequency region, the ν_2 region suffers from spectral crowding with Soret excitation and ν_3 is less sensitive to porphyrin nonplanarity than ν_{10}. Assuming that each of the four hemes has an equal contribution to the intensity,

we resolved ν_{10} and ν_3 into four sublines with equal areas (Table 3). The Raman spectra and results of the spectral decomposition of ν_{10}, along with the amount of ruffling of the four hemes, are illustrated in Figure 7. The frequencies, line widths, and uncertainties for the sublines are summarized in Table 3. A potential problem arises with this approximation if the absorption spectra of the individual hemes differ significantly, and consequently, the resonance enhancement of the hemes differs markedly. However, the individual bands are not shifted by the <1 Å heme distortions by enough to significantly broaden the Soret absorption. Further Raman spectra taken at 413.1 nm excitation indicate that resonance enhancement differences introduce errors less than the possible statistical error in the curve-fitting results for spectra taken at 406.7 nm. In fact, if the assumption of equal areas is correct, the same band profile will emerge, and that is indeed the case (spectra not shown). The 413.1 nm spectral decomposition data is included in Table 3. The decomposition results for ν_3 are given to demonstrate the consistency of the spectral decompositions for different structure-sensitive lines.

For model metal porphyrins (*14*, *19*, *40*) and for some heme proteins (*46*), structural heterogeneity causes complex line shapes for the structure-sensitive Raman lines, especially for ν_{10}. In making the assumption that heterogeneity does not play a role, we implicitly apply the direct observation that the range of ruffling that is observed in a particular c_3 protein matches the range of frequencies apparent in the Raman line shape. In fact, the standard deviation in the ruffling of the four hemes correlates with the overall line width of ν_{10}. This connection between the Raman data and NSD results is visible to the unaided eye in Figure 7; for the proteins for which there is a narrow distribution of rufflings of the heme, a broad but fairly symmetric line is observed. On the other hand, when a broad distribution for ruffling is seen, the line is very broad and asymmetric. Nonetheless, conformational heterogeneity could play a role in the complex line shapes seen in the Raman data. Such heme heterogeneity does influence the line shapes of the structure sensitive lines of cytochromes c_2 (*46*), but we suspect that the structural heterogeneity in this case is special. For cytochromes c_2, heme structural heterogeneity is also apparent in the normal-coordinate structural decomposition of the hemes of the crystal structures that are available (*9*), but not for most other *c*-type cytochromes. In addition, the distortions for cytochromes c_2 are much smaller than for the cytochromes c_3, the H-bonding in the fingerprint peptide is weaker, and thus the hemes may have more flexibility.

From the NSD and MM calculations, the largest differences in the conformations of hemes of the cytochromes c_3 are found in hemes 4. Specifically, the hemes of the *baculatum* cytochromes c_3 are mainly ruffled while the other proteins show a strong heme saddling. First, we notice that the frequencies of the lines, including ν_4, ν_3, and ν_2, of the *baculatum* cytochromes c_3 are lower than those of the proteins from the other strains (see Table 2). This is consistent with a more nonplanar heme, or, alternatively, since there are four hemes, one or all of the hemes may be more nonplanar. In addition, a shoulder that appears on the low-frequency side of ν_{10} in the spectra of the *baculatum* strains (see Figure 7) indicates that one or a fraction of the hemes is significantly less planar than the others. The differences in the heme conformation between the *baculatum* cytochromes c_3 and the proteins from the other strains are also evident in the line-shape changes of ν_8 and many other lines in the low-frequency region (not shown) (*45*).

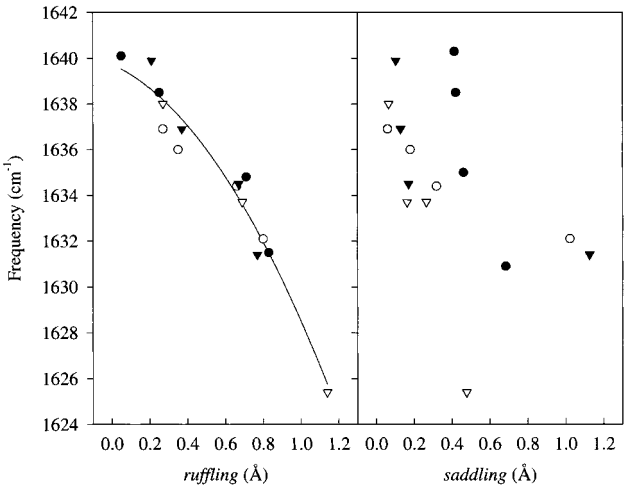

FIGURE 8: Correlation of the frequencies of the sublines of ν_{10} with the *ruf* (right panel) and *sad* (left panel) deformations of each of four hemes in the X-ray crystal structures of cytochromes c_3 from strains *D. gigas* (●), *D. vulgaris* Hildenborough (○), *D. desulfuricans* ATCC 27774 (▼), and *Dsm. baculatum* Norway 4 (▽).

As can be seen from Figure 7, the most obvious difference between the spectra of the *baculatum* strains and that of the other proteins is that the lowest frequency subline has a much lower frequency for the *baculatum* strains than for the others. This indicates a more distorted heme for the *baculatum* strains than for the other cytochromes c_3. Detailed comparison of the Raman data with the NSD results allows us to determine which of the four hemes is associated with each subline and, thus, identify which heme is associated with the anomalously low-frequency subline of the *baculatum* strain.

From model compound studies, we know that more distorted porphyrins exhibit lower frequencies for the structure-sensitive marker lines (*17*, *35*). If we assume the ruffling is the important deformation in causing the downshift in the Raman lines, we can assign the lowest-frequency subline to the most ruffled heme and so forth for the other hemes. The frequencies of the sublines are then plotted versus the amount of ruffling of the hemes in the X-ray crystal structures to see if this type of deformation gives a consistent set of correlations with the Raman frequencies for all of the proteins. We can then independently carry out this procedure for the other types of heme deformations. The resulting correlations of the frequencies with the amount of ruffling and saddling are shown in Figure 8. A good correlation is found if we plot the frequencies with the *ruf* deformation ($r^2 = 0.95$). The same procedure for the *sad* deformation gives no correlation (Figure 8, right panel). The correlation between the frequencies and the total distortion, which primarily reflects the large *ruf* and *sad* deformations, is much worse ($r^2 = 0.79$) than the corresponding correlation with ruffling alone. This suggests that ruffling is the dominant factor that influences the structure-sensitive Raman lines. Figure 9 shows that ν_3 exhibits similar dependencies on saddling and ruffling, with a correlation ($r^2 = 0.90$) only in the case of ruffling. These results suggest that even large saddling has little or no effect on these modes.

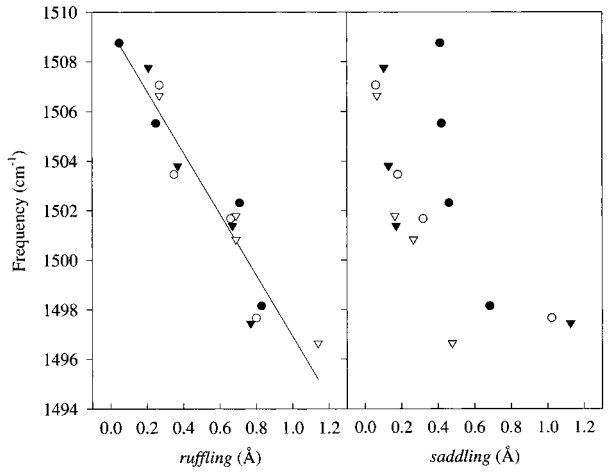

FIGURE 9: Correlation of the frequencies of the sublines of ν_3 with the *ruf* (right panel) and *sad* (left panel) deformations of each of four hemes in the X-ray crystal structures of cytochromes c_3 from strains *D. gigas* (●), *D. vulgaris* Hildenborough (○), *D. desulfuricans* ATCC 27774 (▼), and *Dsm. baculatum* Norway 4 (▽).

There is other evidence from studies of model nonplanar porphyrins (*47*) corroborating the weaker sensitivity of ν_{10} and ν_3 to saddling compared to ruffling. An analysis of the Raman spectra and structural data for ruffled nickel *meso*-tetraalkylporphyrins (*17*) and mostly saddled nickel octaalkyl-*meso*-tetraphenyl-porphyrins (*35*) shows that saddling has much less influence on the frequencies of the structural marker lines. Specifically, ν_4, ν_3, and ν_2 show between 5 and 20 times small dependence on saddling than on ruffling (*47*). Unfortunately, ν_{10} is not observed for these porphyrins, but for other porphyrins the frequency dependence of ν_{10} on distortion is similar to that of ν_3. Furthermore, decomposition of ν_3 gives almost the same results as obtained for ν_{10} for the cytochromes c_3. The weak frequency dependence on saddling might have been expected based on the preeminence of $C_\alpha-C_{meso}$ stretching in the potential-energy distribution of these marker lines. Ruffling causes considerable twisting about the $C_\alpha-C_{meso}$ bond, whereas saddling does not. Resonance Raman studies designed to identify lines that are selectively sensitive to saddling would be useful.

On the basis of both the model compound results and the correlations in Figure 8, we assign the sublines of ν_{10} to specific hemes in the X-ray structures of the cytochromes c_3. The more ruffled the heme (longer bar), the lower the frequency of the subline. In the case of the *baculatum* proteins (Norway 4 and 9974), the distinctive spectra are a consequence of the excessive ruffling of hemes, especially hemes 2 which gives the large downshift for the lowest frequency subline.

The above analysis also has some value in predicting structures and spectra. For instance, the heme ruffling for the proteins whose crystal structures are not known can be predicted by analyzing the line shape of ν_{10} and then applying the correlation given in Figure 8. As examples, the predicted ruffling of the hemes of cytochromes c_3 from *D. desulfuricans* Essex 6 and *Dsm. baculatum* 9974 are given in Figure 7 (hemes 2 > hemes 1, 4 > hemes 3).

We can also predict the Raman spectrum of the structure-sensitive lines of the *baculatum* strain (NCIB 8310) for which data is not available. On the basis of the NSD of the crystal structures of the native and mutant proteins, the Raman spectra should look much more like the other proteins than Norway 4. This is because the magnitude of the ruffling of heme 4 is closer to that of the *desulfuricans* and *vulgaris* strains and because the ruffling of heme 2 is more in line with the other proteins.

Effects of the Fingerprint Peptide Segment on Heme Distortions. For *c*-type cytochromes, the fingerprint sequence −Cys−X_1−X_2−Cys−His− (or −Cys−X_1−X_2−X_3−X_4−Cys−His−) is largely responsible for the distortion of the heme group (*8, 20*). Analysis of the influence of natural sequence variation and engineered mutations for *c*-type cytochromes suggests that the structural origin of the heme distortion is most likely concentrated in this small segment of the protein (*8*). RR studies and MM calculations for nickel(II) cytochrome *c* and model compounds further support this hypothesis (*20*). Specifically, pH unfolding of the secondary structure leads to a less distorted macrocycle presumable because the structure of this peptide segment is relaxed. Clearly, the MM calculations and NSD results for hemes 1, hemes 2, and hemes 4 of cytochromes c_3 from different strains show that the fingerprint peptide segment alone is enough to induce the main deformations contributing to the distortions of these hemes.

For hemes 3, the total distortion is smaller than for the other three hemes, and the fingerprint peptide segment by itself induces a distortion different from that of the crystal structure. However, adding the sixth ligand and fixing propionate oxygens in the calculations make the conformation close to that of the crystal structure. This implies that, for the hemes with relatively small distortions, not only the fingerprint peptide segment but also the sixth ligand, the hydrogen bonds with the heme propionates, and, indeed, van der Waals contacts with the rest of the protein, all influence the heme conformation.

For hemes 1, when the perturbations of the sixth ligand and the fixed propionates are applied in the calculation, the structures become less distorted and the agreement with the X-ray structure gets worse. However, energy optimization of the heme with the whole protein fixed gives a heme conformation that is very close to that of the crystal structure (see Figure 10), implying that many heme contacts appear to have an influence. Some proteins, e.g., the peroxidases, exhibit large nonplanar heme distortions (∼1 Å) in the absence of covalent links between the heme and the protein. In this case, the *only* mechanisms of distortion is through the van der Waals contacts and the axial ligands. Thus, it is not too surprising to find a heme in a *c*-type cytochrome for which these interactions are also a major factor. Nonetheless, when all of the interactions are included, the correct heme structure is calculated (Figure 10). Still, since the fingerprint peptide of heme 1 alone gives approximately the correct structure, it must still contribute strongly to the heme conformation observed in the X-ray structure.

On the other hand, for the highly distorted hemes 2 and 4, addition of these structural perturbations has little further effect. Higuchi and co-workers (*4*) suggest that the heme puckering is not related to the number of residues inserted between the cysteine residues for hemes 4 but is probably caused by the steric hindrance imposed by the bulky side chains around the hemes. Our work agrees with this conclusion in its simplest form, i.e., the number of amino

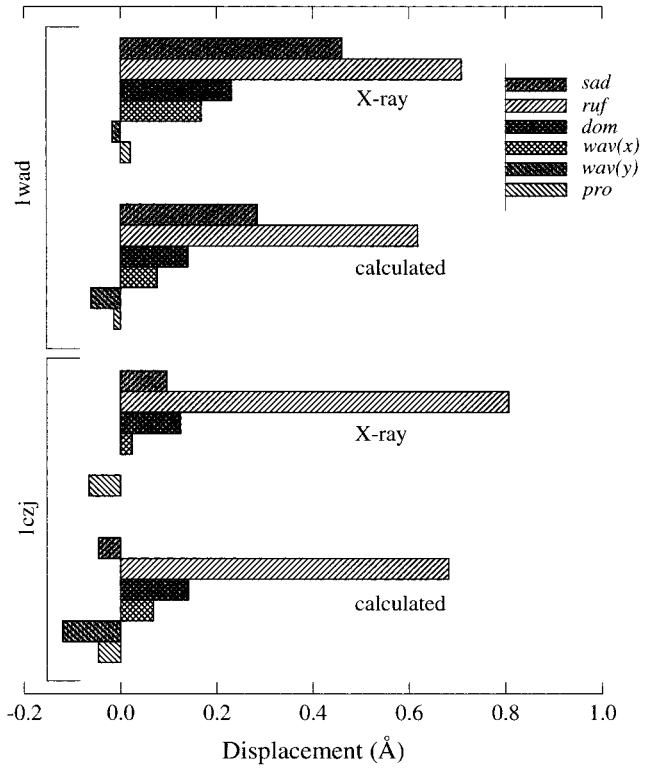

FIGURE 10: Out-of-plane displacements (minimal basis) for hemes 1 in the X-ray crystal and energy-optimized structures of cytochromes c_3 from strain *D. gigas* (1wad) *and Dsm. baculatum* Norway 4 (cc3) (1czj). The energy-optimized structures were obtained by minimization of the whole protein.

acids alone does not determine the heme structure. However, stated in a more general way, the *conformation* of the fingerprint segment structure does largely determine the heme structure, and the number of amino acids has a large influence on conformation of the segment. Except possibly in the case of hemes 1, our work strongly indicates the primary role of the fingerprint peptide. Furthermore, the deletion of two residues between the cysteines for the *baculatum* strain makes the conformation of hemes 4 different from that for other strains. Although the conformational change of hemes 4 of the *baculatum* strain may not be simply ascribed to change in the number of residues between the cysteines, the number certainly changes the folding of the fingerprint peptide segment. Furthermore, MM calculations suggest that the van der Waals contacts between the fingerprint peptide and the heme play a major role. This is demonstrated by calculations in which the peptide is deleted and the heme-peptide attachment points are fixed. In these calculations the heme minimizes to a nearly planar conformation despite the constraints (*48*). Thus, it is not simply the difference in the number of amino acids, but the resulting differences in the folding of the fingerprint peptide and the consequent differences in the peptide-heme contacts that are important in determining the heme structure.

Correlations between Heme Structure and Fe Reduction Potentials. In most cases, no simple relationship between metal reduction potentials and either heme Raman frequencies or nonplanar distortion is found (*49*). However, an *influence* of heme nonplanarity on redox potentials *is* expected because model porphyrin studies have shown such an effect on ring redox potentials (*11, 22*). For metal redox centers, a number of other influences can obscure this dependence. For example, differences in axial ligation (ligand orientation, H-bonding of axial ligands to protein, etc.) can occur, and these differences will influence potentials. In addition, it is not clear how Fe reduction potentials are influenced by nonplanarity since model compound studies have focused mainly on porphyrin ring potentials.

Table 4: Heme Assignments for *D. gigas*, *D. vulgaris*, and *Dsm. baculatum* Tetraheme Cytochromes c_3 Based on the Magnitude of Ruffling and Other Properties[a] (*50*)

	redox potentials			
organism	e1	e2	e3	e4
D. gigas[a]	h1	h2	h3	h4
ruffling	h2	h1	h3	h4
total distortion	h2	h1	h4	h3
D. vulgaris[a]	h3	h2	h1	h4
ruffling	h2	h1	h4	h3
total distortion	h4	h2	h1	h3
Dsm. baculatum[a]	h2	h1	h4	h3
ruffling	h2	h1 or h4	h4 or h1	h3
total distortion	h2	h4	h1	h3

[a] Self-consistent global assignments based on X-ray structural data for histidine ligand orientation, EPR, chemical modification, and degree of exposure to solvent (*50*).

Nevertheless, it is interesting to predict the ordering of redox potentials based solely on the magnitude of ruffling and compare this to previous attempts to assign specific hemes to the redox potentials. The potentials of the hemes vary from about −350 to −70 mV. Table 4 gives the heme assignments to the measured redox potentials (increasing in the order e1 < e2 < e3 < e4) based on ruffling and on total heme distortion. These assignments should be compared to previous self-consistent global assignments based on three methods, including EPR data and X-ray data for the orientation of the histidine ligands, chemical modification, and the degree of heme solvent exposure (*50*). These assignments are also given in Table 4. Given the ambiguity in the global assignments, the agreement of assignments based on distortion is generally consistent with those based on other considerations. Thus, ruffling probably enhances the effect of these other properties in lowering the potentials of the hemes.

SUMMARY AND CONCLUSIONS

The nonplanarity of the hemes in cytochromes c_3 is mainly caused by a fingerprint peptide segment including two cysteines, the amino acids between the cysteines, and the proximal histidine. The histidine sixth ligand and interactions between the heme propionates and the rest of the protein influence the heme conformation to a lesser extent. Factors that influence the folding pattern of the fingerprint peptide segment and other peptide-heme contacts also influence the heme conformation. Some of the structural differences between cytochromes c_3 of the *baculatum* strain and other strains that are uncovered by the NSD results for the X-ray structures are also observed in the RR spectra. The overall frequencies of the structure-sensitive lines (ν_4, ν_3, and ν_2) in the high-frequency region of the RR spectra are lower for *Dsm. baculatum* (Norway 4 and 9974) cytochromes c_3 than those for *D. gigas*, *D. vulgaris*, and *D. desulfuricans*, consistent with a more ruffled heme. Spectral decomposi-

tions of the structure-sensitive lines ν_3 and ν_{10} indicate that ruffling rather than saddling is the dominant factor in determining the frequencies, in agreement with model compound Raman and X-ray structural data. The distinctive spectra of the *baculatum* proteins are a consequence of hemes 2 and 4 being excessively ruffled. On the basis of the ruffling in the X-ray structures, the hemes can be assigned to sublines in the Raman line shapes and to the reported microscopic redox potentials.

ACKNOWLEDGMENT

We thank Prof. Mark R. Ondrias at University of New Mexico for helpful discussions and comments on the manuscript. We thank Drs. Oliver Einsle, Stefanie Foerster and Albrecht Messerschmidt (Max-Planck Institute für Biochemie, Martinsried, Germany) for X-ray structure data for *D. desulfuricans* (Essex 6).

REFERENCES

1. Matias, P. M., Morais, J., Coelho, R., Carrondo, M. A., Wilson, K., Dauter, Z., and Sieker, L. (1996) *Protein Sci. 5*, 1342−1354.
2. Morimoto, Y., Tani, T., Okumura, H., Higuchi, Y., and Yasuoka, N. (1991) *J. Biochem. 110*, 532−540.
3. Matias, P. M., Frazao, C., Morais, J., Coll, M., and Carrondo, M. A. (1993) *J. Mol. Biol. 234*, 680−699.
4. Higuchi, Y., Kusunoki, M., Matsuura, Y., Yasuoka, N., and Kakudo, M. (1984) *J. Mol. Biol. 172*, 109−139.
5. Morais, J., Palma, P. N., Frazao, C., Caldeira, J., LeGall, J., Moura, I., Moura, J. J. G., and Carrondo, M. A. (1995) *Biochemistry 34*, 12830−12841.
6. Czjzek, M., Payan, F., Guerlesquin, F., Bruschi, M., and Haser, R. (1994) *J. Mol. Biol. 243*, 653−667.
7. Czjzek, M., Guerlesquin, F., Bruschi, M., and Haser, R. (1996) *Structure 4*, 395−404.
8. Jentzen, W., Ma, J.-G., and Shelnutt, J. A. (1998) *Biophys. J. 74*, 753−763.
9. Shelnutt, J. A., Song, X.-Z., Ma, J.-G., Jia, S.-L., Jentzen, W., and Medforth, C. J. (1998) *Chem. Soc. Rev. 27*, 31−41.
10. Geno, M. K., and Halpern, J. (1987) *J. Am. Chem. Soc. 109*, 1238−1240.
11. Barkigia, K. M., Chantranupong, L., Smith, K. M., and Fajer, J. (1988) *J. Am. Chem. Soc. 110*, 7566−7567.
12. Furenlid, L. R., Renner, M. W., Smith, K. M., and Fajer, J. (1990) *J. Am. Chem. Soc. 112*, 1634−1635.
13. Furenlid, L. R., Renner, M. W., Smith, K. M., and Fajer, J. (1990) *J. Am. Chem. Soc. 112*, 8987−8989.
14. Alden, R. G., Ondrias, M. R., and Shelnutt, J. A. (1990) *J. Am. Chem. Soc. 112*, 691−697.
15. Tetreau, C., Lavalette, D., Momenteau, M., Fischer, J., and Weiss, R. (1994) *J. Am. Chem. Soc. 116*, 11840−11848.
16. Jentzen, W., Song X.-Z., and Shelnutt, J. A. (1997) *J. Phys. Chem. B 101*, 1684−1699.
17. Jentzen, W., Simpson, M. C., Hobbs, J. D., Song, X., Ema, T., Nelson, N. Y., Medforth, C. J., Smith, K. M., Veyrat, M., Mazzanti, M., Ramasseul, R., Marchon, J.-C., Takeuchi, T., Goddard, W. A., III, and Shelnutt, J. A. (1995) *J. Am. Chem. Soc. 117*, 11085−11097.
18. Hobbs, J. D., and Shelnutt, J. A. (1995) *J. Protein Chem. 14*, 19−25.
19. Anderson, K. K., Hobbs, J. D., Luo, L., Stanley, K. D., Quirke, J. M. E., and Shelnutt, J. A. (1993) *J. Am. Chem. Soc. 115*, 12346−12352.
20. Ma, J.-G., Laberge, M., Song, X.-Z., Jentzen, W., Jia, S.-L., Zhang, J., Vanderkooi, J. M., and Shelnutt, J. A. (1998) *Biochemistry 37*, 5118−5128.
21. Othman, S., Lirzin, A. L., and Desbois, A. (1994) *Biochemistry 33*, 15437−15448.
22. Ravikanth, M., and Chandrashekar, T. K. (1995) *Struct. Bonding 82*, 105−188.
23. Nivière, V., Hatchikian, E. C., Bianco, P., and Haladjian, J. (1988) *Biochim. Biophys. Acta 935*, 34−40.
24. Benosman, H., Asso, M., Bertrand, P., Yagi, T., and Gayda, J. P. (1989) *Eur. J. Biochem. 182*, 51−55.
25. Mus-Veteau, I., Dolla, A., Guerlesquin, F., Payan, F., Czjzek, M., Haser, R., Bianco, P., Haladjian, J., Rapp-Giles, B. J., Wall, J. D., Voordouw, G., and Bruschi, M. (1992) *J. Biol. Chem. 267*, 16851−16858.
26. Bruschi, M., Loufti, R., Bianco, P., and Haladjian, J. (1984) *Biochem. Biophys. Res. Commun. 120*, 384−389.
27. Moura, I., Teixeira, M., Huynh, B. H., LeGall, J., and Moura, J. J. G. (1988) *Eur. J. Biochem. 176*, 365−369.
28. Guigliarelli, B., Bertrand, P., More, C., Haser, R., and Gayda, J. P. (1990) *J. Mol. Biol. 216*, 161−166.
29. LeGall, J., Mazza, G., and Dragoni, N. (1965) *Biochim. Biophys. Acta 99*, 385−387.
30. DerVartanian, D. V., and LeGall, J. (1974) *Biochim. Biophys. Acta 346*, 79−99.
31. Liu, M.-C., Costa, C., Coutinho, I. B., Moura, J. J. G., Moura, I., Xavier, A. V., and LeGall, J. (1988) *J. Bacteriol. 170*, 5545−5551.
32. Bruschi, M., Hatchikian, L. E., Golovleva, L. A., and LeGall, J. (1977) *J. Bacteriol. 129*, 30−38.
33. Shelnutt, J. A. (1983) *J. Phys. Chem. 87*, 605−616.
34. Mayo, S. L., Olafson, B. D., and Goddard, W. A., III (1990) *J. Phys. Chem. 94*, 8897−8909.
35. Shelnutt, J. A., Medforth, C. J., Berber, M. D., Barkigia, K. M., and Smith, K. M. (1991) *J. Am. Chem. Soc. 113*, 4077−4087.
36. Li, X.-Y., Czernuszewics, R. S., Kincaid, J. R., and Spiro, T. G. (1989) *J. Am. Chem. Soc. 111*, 7012−7023.
37. Li, X.-Y., Czernuszewics, R. S., Kincaid, J. R., Su, Y. O., and Spiro, T. G. (1990) *J. Phys. Chem. 94*, 31−47.
38. Li, X.-Y., Czernuszewics, R. S., Kincaid, J. R., Stein, P., and Spiro, T. G. (1990) *J. Phys. Chem. 94*, 47−61.
39. Song, X.-Z., Jentzen, W., Jia, S.-L., Jaquinod, L., Nurco, D. J., Medforth, C. J., Smith, K. M., and Shelnutt, J. A. (1996) *J. Am. Chem. Soc. 118*, 12975−12988.
40. Alden, R. G., Crawford, B. A., Doolen, R., Ondrias, M. R., and Shelnutt, J. A. (1989) *J. Am. Chem. Soc. 111*, 2070−2072.
41. Jentzen, W., Unger, E., Karvounis, G., Shelnutt, J. A., Dreybrodt, W., and Schweitzer-Stenner, R. (1996) *J. Phys. Chem. 100*, 14184−14191.
42. Jentzen, W., Unger, E., Song, X.-Z., Jia, S.-L., Turowska-Tyrk, I., Schweitzer-Stenner, R., Dreybrodt, W., Scheidt, W. R., and Shelnutt, J. A. (1997) *J. Phys. Chem. A 101* 5789−5798.
43. Sparks, L. D., Medforth, C. J., Park, M.-S., Chamberlain, J. R., Ondrias, M. R., Senge, M. O., Smith, K. M., and Shelnutt, J. A. (1993) *J. Am. Chem. Soc. 115*, 581−592.
44. Hu, S.-Z., Morris, I. K., Singh, J. P., Smith, K. M., and Spiro, T. G. (1993) *J. Am. Chem. Soc. 115*, 12446−12458.
45. Ma, J.-G., Zhang, J., Franco, R., Jia, S.-L., Moura, I., Moura, J. J. G., Kroneck, P. M. H., and Shelnutt, J. A. (Manuscript in preparation).
46. Othman, S., Fitch, J., Cusanovich, M. A., and Desbois, A. (1997) *Biochemistry 36*, 5499−5508.
47. Ma, J.-G., Jia, S.-L., and Shelnutt, J. A. unpublished results.
48. Ma, J.-G., Laberge, M., Zhang, J., Jia, S.-L., Vanderkooi, J. M., and Shelnutt, J. A. (Manuscript in preparation).
49. Othman, S., Richaud, P., Verméglio, A., and Desbois, A. (1996) *Biochemistry 35*, 9224−9234.
50. Coutinho, I. B., and Xavier, A. V. (1994) *Methods Enzymol. 243*, 119−140.

BI981189I